Supplementary Information for

Infrared and Reflectron Time-of-Flight Mass Spectroscopic Study on the Synthesis of Glycolaldehyde in Methanol (CH_3OH) and Methanol -- Carbon Monoxide (CH_3OH-CO) Ices Exposed to Ionization Radiation

Surajit Maity, Ralf I. Kaiser,* Brant M. Jones*

W. M. Keck Research Laboratory in Astrochemistry, University of Hawaii at Manoa, Honolulu, Hawaii, HI, 96822, USA

Department of Chemistry, University of Hawaii at Manoa, Honolulu, Hawaii, HI, 96822, USA

Email addresses: ralfk@hawaii.edu (R. I. K.)
brantmj@hawaii.edu (B. M. J.)

SI Experimental:

Vacuum Ultraviolet Light Generation

Pulsed coherent vacuum ultraviolet (VUV) light at 118.2 nm (10.49 eV) was generated exploiting a nonlinear four wave mixing process ($\omega_{vuv} = 3\omega_1$) utilizing xenon as the nonlinear medium.[1-3] Briefly, the mechanism behind non-linear four wave mixing is described below. The polarizability of a material in a weak electric field may be ascribed by a simple linear relationship,

$$\vec{P} = \epsilon_0 \chi \vec{E} \quad (2)$$

However, in the presence of an intense electric field, higher order non-linear terms must be considered:

$$\vec{P} = \epsilon_0 \left(\chi^{(1)} \vec{E} + \chi^{(2)} \vec{E}^2 + \chi^{(3)} \vec{E}^3 + \cdots \right) \quad (3)$$

If we considered a simple and very intense propagating electromagnetic wave with frequency ω_1,

$$E = E_0 cos(\omega_1 t) \quad (4)$$

then

$$\vec{P} = \epsilon_0 \left(\chi^{(1)} E_0 cos(\omega_1 t) + \chi^{(2)} E_0 cos(\omega_1 t)^2 + \chi^{(3)} E_0 cos(\omega_1 t)^3 + \cdots \right) \quad (5)$$

From here, the third order cosine can be reduced using the power reducing trigonometry identity,

$$cos^3(\theta) = \frac{3\cos(\theta) + \cos(3\theta)}{4} \quad (6)$$

giving a term in P as

$$\frac{1}{4} \varepsilon_0 E_0 \cos(3\omega_1 t) \quad (7)$$

Essentially, a very intense electromagnetic field can induce an ensuing field in a medium with a non-zero third order electric susceptibility $\chi^{(3)}$ oscillating at three times the input frequency. Here, ω_1 is the third harmonic (354.6 nm) output of a high power pulsed neodymium-doped yttrium aluminum garnet laser (Nd:YAG, Spectraphysics, PRO-250) operated at 30 Hz. Typical operating values for the fundamental (ω_1) at 0.8 W or 27 mJ per pulse. The pulsed xenon gas jet was housed in a separated mixing chamber evacuated by a 400 l s^{-1} turbomolecular pump. The pulsed valve fired 286 µs prior to the Q-switch of the Nd:YAG laser. The timing sequence is shown in Figure S1. The optimization of the pulsed valve timing with respect to the Q-switch of Nd:YAG laser is depicted in Figure S2. The pulsed valve was connected to the middle entrance of a T shape channel with a 1 mm diameter at 25 mm in length whereupon, xenon (Specialty Gases of America, 99.999%) from the pulsed valve entered the T shape adapter thereby forming an instan-

taneous pulsed mixing cell in line with the propagating ω_1 pulse. Nominal operating pressures during VUV generation are on the order of 4×10^{-4} torr with the generation chamber with the pulse valve maintained at a xenon backing pressure of 2.7 atm (Figure S3), derived from empirical optimization. The ω_1 laser beam was empirically focused into a T-shaped adapter on the valve to yield optimal VUV intensity. Separation of the ω_1 fundamental (354.6 nm, 3.496 eV) from generated ω_{VUV} (118.2 nm, 10.49 eV) beam was accomplished using an off axis LiF plano-convex lens[4] (ISP Optics, LF-PX-38-150) (Figure S4). The separation lens was differentially pumped to maintain ultra-high vacuum conditions (~10^{-11} torr) within the main chamber while being coupled to the VUV mixing chamber (~10^{-4} torr). Here, the LiF lens was mounted in a flat stainless steel plate that was then sealed with two parallel plates, (with a one inch diameter hole in the center) holding concentric O-rings with different inner diameters on both sides. A small port in between the two O-rings of each plate was drilled through and coupled with corresponding vacuum fittings that allowed the evacuation via a small turbo molecular pumping station (Balzer TSU 071). This setup allows the lens to move horizontally in a direction that is perpendicular to the propagating ω_1 and ω_{VUV} beam axis, while constantly being evacuated to typical pressures of 10^{-8} torr. The separation lens housing was then connected to the main chamber with a port alignment flange (MDC Vacuum, 675002) and a standard nipple with a 0.5 cm hole drilled into a solid copper gasket evacuated by a separate turbo molecular pump with typical operating pressures of 10^{-10} torr. The solid copper gasket served two functions in that it aided in blocking out the fundamental ω_1 beam and assisted in differential pumping allowing for the maintained UHV conditions in the main chamber. In addition, the entire VUV generation chamber was rotated about 5^o to compensate for the deflection angle of the lithium fluoride (LiF) separation lens for the generated VUV beam. Two detectors we used in order to monitor and optimize the generated VUV light, and to ensure proper alignment through the main chamber; these detectors operate on the photoelectric principle and were constructed of high purity OFHC copper consisting of one solid disk (diameter of 1.25 cm, thickness of 0.38 cm) coupled to a ring (inner diameter of 0.5 cm) with ceramic insulators separated by a distance of 0.2 cm. A voltage of 350 V is applied to the ring; once the VUV photons hit the solid copper disk, electrons are then ejected and collected via the ring with the supplied voltage. The detector response as a function of applied voltage as shown in Figure S5, with a fit described by

$$V_p = 1.26\text{-}1.3e^{-.007(Vr)} \qquad (8)$$

The pulsed voltage induced from the collected current is then monitored on digital oscilloscope with typical values at 900 mV with a 4 ns pulse width; see Figure S6 for a typical response curve of the detector. Utilizing this information while assuming total collection efficiency with no additional secondary electrons from spurious plasma generation, we can estimate the amount of VUV photons per pulse at about 10^{14} photons per pulse.

Reflectron Time-of-Flight

The reflectron time-of-flight spectrometer (Jordan TOF Products, Inc.) with customized electrostatic lens setup for the ion source assembly was used to monitor the arrival times of the endogenous formed products as they sublimate into the gas phase. Typically, ions are extracted into the focusing region with a repeller plate (positive voltage) and an extraction plate (negative voltage). Here, the silver target represents the repeller plate. However, as the silver target is directly mounted to the copper cold finger with indium foil to ensure thermal conductivity, no voltage can be applied to the silver target without floating the entire chamber as they have a common ground. An initial attempt was made at coupling the substrate to the cold finger utilizing a thin (0.5 mm) sapphire crystal to electorally isolate the substrate and consequently float at a small positive voltage. However, the inherit nonlinear thermal conductivity of sapphire at cryogenic temperatures[5, 6] resulted in spurious and inconsistent thermal desorption profiles in the temperature regime from 5 K to 40 K. To overcome this, the field between the repeller and extractor plate was simply held at an overall negative potential. Once the molecules sublimate into the gas phase, they are then ionized by the VUV light source (10.49 eV) and then resolved by mass to charge ratio utilizing reflectron time-of-flight mass spectrometry. The ions are detected utilized a multichannel plate with a dual chevron configuration. From the here the signals were amplified using a fast preamplifier (Ortec 9305) and shaped with a 100 MHz discriminator. The TOF spectra were recorded with a personal computer based multichannel scaler (FAST ComTec, P7888–1 E) using a bin width of 4 ns. Calibration of the reflectron was done with the following molecules, representing a very reasonable mass range: ammonia (NH_3), hydrogen sulfide (H_2S), allene (C_3H_4), propene (C_3H_6), 1,3-butadiene (C_4H_6), n-butane (C_4H_{10}), n-pentane (C_5H_{12}), n-hexane (C_6H_{14}), vinyl bromide (C_2H_3Br), and iodotrifluoromethane (CF_3I) was well as their isotopologues, Figure S7. Although molecular hydrogen has an ionization energy of 15.42 eV, we attribute signal at 3940 μs arrival time based on the observation that this

peak increased linearly with corresponding background pressure of molecular hydrogen bled into the main chamber. The ionization of this molecule must be a non-resonant multiphoton absorption process through the Lyman band ($X\ ^1\Sigma_g^+ \rightarrow B\ ^1\Sigma_u^+$) of molecular hydrogen.[7]

CASINO - Electron Trajectory Simulations

We utilize the latest version of CASINO (v2.42) to simulate the interaction of electrons with the methanol and the carbon monoxide – methanol ices.[8] A simulation was performed for pure amorphous methanol (CH_3OH) with a thickness 510 nm as derived from the *in situ* laser interferometry and for the methanol-carbon monoxide (CH_3OH-CO) mixed layer with thickness of 495 nm again determined from laser interferometry. In order to run the simulation, CASINO requires *a priori* knowledge of the densities and composition. Here, the density of amorphous methanol was taken from literature values reported at 1.020 g cm^{-3}. For the binary mixture, the density was calculated based on the weighted average of the pure densities relative to the ratios (as determined from the derived column densities) of each component (ρ_{CO} = 1.029 g cm^{-3}) assuming volume additivity, yielding a value of 1.026 g cm^{-3}. Estimating the density of mixed ices following this technique has been demonstrated previously by Luna et al,[9] as a reasonable approximation to within 20 % or their expected values. Within CASINO is "The Virtual Scanning Electron Microscope" i.e., the source of electrons and was set with physical parameters according to the experimental conditions. Specifically, electrons with kinetic energy of 5 keV simulated striking the surface of sample layer at an angle of 70^0 relative to surface normal. A total number of 10^6 electrons were used to simulate electron trajectories with the default physics model; for a more complete description of the options see Drouin et al..[8] Results of the simulation of are compiled and shown in Figure S8. Specifically, Figure S8(A) and S8(E) display the absorbed energies of the penetrating electrons in the CH_3OH and CH_3OH-CO ices, respectively. Further, we can obtain information about the maximum penetration depth of the electrons in the sample (Figure S8(B) and S8(F)), the average energy of transmitted electrons (Figure S8(C) and 2G) and the average energy and percentage of the electrons backscattered from the incident surface (Figure S8(D) and S8(H)). Note that, the maximum penetration depth of the electrons, 252 ± 10 nm and 265 ± 10 nm in CH_3OH and CH_3OH-CO ices, respectively, are less than total thickness of the samples (510 nm for CH_3OH and 495 nm for CH_3OH-CO ices), as such the interaction of the electrons are predominantly within the bulk ice and not with the substrate. In

the case of CH_3OH sample, the total energy transmitted *through* the sample per incident electron was calculated at 0.008 ± 0.001 keV with only about 1% of the incoming electrons travelling completely *through* the ice. Due to the relatively shallow angle, some of the electrons are scattered off with an energy loss. Here, approximately 33 ± 5 % of total number of electrons are scattered from the surface with an energy of 1.06 ± 0.16 keV per incident electron. This leads to energy of 4.65 ± 0.32 keV per electron transferred to the methanol ices. From here, the dose per molecule can be calculated from the density, irradiation area, thickness, and total number of electrons yielding a value of 6.5 ± 0.8 eV per CH_3OH molecule. Similarly, CASINO results for the CH_3OH-CO ice sample yield about 1% of the total number of electrons with total energy of 0.029 ± 0.008 keV per electron are transmitted, along with 35 ± 5 % of incoming electrons with a total energy of 1.1 ± 0.2 keV per electron are backscattered; which leads to an energy transfer of 4.60 ± 0.31 keV per electron to the methanol-carbon monoxide ices. The dose is then calculated as 5.2 ± 0.8 eV per molecule. In order to estimate the dose per molecule for a binary mixture, we utilized the derived column density of each constituent with the irradiated area to calculate the total number of respective molecules.

SI Results:
Warm-up Phase

Changes of the infrared absorptions attributed to the carbonyl functional group of glycolaldehyde identified above during the warm-up phase are monitored to ascertain the fate of this complex organic as a function of temperature, thereby simulating the transition from the cold molecular cloud to star forming regions. Here, the corresponding change of the carbonyl absorption features in the region of 1900–1600 cm^{-1} in irradiated methanol and methanol-carbon monoxide ices are shown in Figure S9 and S10 respectively with the integrated band areas of the identified infrared absorption (deconvoluted) bands during the warm-up phase displayed in Figure S11. The abundances of glycolaldehyde in methanol and methanol-carbon monoxide ices during the irradiation phase and during the warm up phase are listed in Table 4 as well. Here, in the irradiated methanol ices, ν_{14} glycolaldehyde fundamental at 1743 cm^{-1} shows an initial increase starting around 25 K until the integrated band area reaches a maximum around 70 K. Considering an integrated absorption coefficient of 2.6 × 10^{-17} cm $molecule^{-1}$ for the ν_{14} glycolaldehyde fundamental,[10] 3.1 ± 0.3 × 10^{14} molecules were produced during the irradiation which is equivalent to a fractional abundance, relative to the initial amount of methanol,

f(CH_3OH) of $1.7 \pm 0.2 \times 10^{-3}$ (0.17 ± 0.02 %) (Table 4). Subsequent heating yields an increase of glycolaldehyde to $8.0 \pm 0.8 \times 10^{14}$ molecules at 70 K which remains unchanged within error limit until 110 K where a somewhat linear decrease is observed where an abundance of $3.2 \pm 0.3 \times 10^{14}$ molecules is reached at 150 K and finally becomes untraceable beyond 175 K. The fractional abundances of glycolaldehyde relative to initial amount of methanol at 110 K and 150 K are $4.4 \pm 0.4 \times 10^{-3}$ (0.44 ± 0.04 %) and $1.8 \pm 0.2 \times 10^{-3}$ (0.18 ± 0.02 %), respectively. The decrease in column density at 110 K is similar to that reported earlier[10] and coincides with a decrease in the column density of methanol (Figure S11) indicating a physical effect of the surrounding methanol matrix cage on the absorption values of the isolated species over a chemical (thermal decomposition) one. At 150 K, glycolaldehyde is sublimating to the gas phase, hence the observed sudden drop in the column density. Note that, immediately following irradiation of methanol ices, $5.3 \pm 0.2 \times 10^{14}$ molecules were calculated for the formyl radical using an integrated absorption coefficient of 1.5×10^{-17} cm molecules^{-1} at 1842 cm^{-1} (ν_3).[10] Formyl radical abundance remains unchanged until 25 K and subsequently becomes untraceable around 100 K within experimental sensitivity limits. Note that a sharp decrease in abundance of the formyl radical was observed until 70 K which correlates strongly to the increase in glycolaldehyde band at 1743 cm^{-1} at 70 K suggesting the presence of additional thermal chemistry between trapped radicals diffusing through the parent matrix during the warm up phase. Within the 25 K to 70 K warm-up phase, the formyl radical shows a decrease in abundance by $4.8 \pm 0.5 \times 10^{14}$ molecules, which is within the error limits of the derived increase in abundance of glycolaldehyde by $4.9 \pm 0.5 \times 10^{14}$ molecules. Therefore, we may suggest that the formyl radicals effectively react to form glycolaldehyde upon warm up of the irradiated ice.

For the irradiated methanol-carbon monoxide ices, the corresponding integrated band areas of the infrared absorption at 1743 cm^{-1} (ν_{14} of glycolaldehyde) and 1842 cm^{-1} (ν_3 of formyl radical) as a function of temperature are depicted in Figure S11. Here, the ν_{14} band of glycolaldehyde displays a pronounced increase in integrated band areas at a temperature range of 110-125 K. In order to identify the origin of this sharp increase, the thermal profiles of the methanol absorption band centered at 1028 cm^{-1}, derived from both the pristine and irradiated methanol-carbon monoxide ices, were plotted and shown in Figure S11. Here, the increase was also observed in the methanol band of the irradiated ice, but not that of the pristine ice. However, both ices exhibited a corresponding phase change of methanol. Accordingly, the sudden increase may be

attributed to the phase change of the methanol at this temperature.[10, 11] A change in physical structure has been shown to alter optical constants (refractive indices and infrared absorption coefficients)[12] and consequently may explain the sudden increase observed of all integrated band areas. However, in the pure methanol irradiated ices, the v_8 band of methanol at 1028 cm^{-1} (Figure S11) does not exhibit any abrupt increase. Here, a slight decrease in infrared absorption was observed starting at ~110 K and gradually continuing until methanol rapidly sublimates at 140 K. The decrease starting at 110 K maybe the top layers of methanol slowly sublimating, whereas the swift decrease at 140 K is the substrate bound methanol sublimating. Recall that, in methanol-carbon monoxide ices, carbon monoxide sublimes at 40 K leaving a more porous ice compared to pure methanol ices.[13] Hence, the drastically different behaviors of these two ices are reasonable.

In the irradiated methanol-carbon monoxide ices, $1.6 \pm 0.1 \times 10^{15}$ glycolaldehyde molecules were produced during the irradiation with a fractional abundance $f(CH_3OH)$ of $1.4 \pm 0.1 \times 10^{-2}$ (1.4 ± 0.1 %) (Table 4). During the warm-up phase, at 50 K the production of glycolaldehyde increased slightly to $1.9 \pm 0.2 \times 10^{15}$ molecules and remains relatively stable within the error limits of the deconvolution. Additionally, the abundance of formyl radical shows a maximum of $1.6 \pm 0.2 \times 10^{15}$ molecules immediately following irradiation where upon it remains stable until 25 K and subsequently cannot be detected beyond 50 K. Within the 25 K to 50 K temperature range, the formyl radical shows a decrease in abundance by $1.6 \pm 0.2 \times 10^{15}$ molecules. During this temperature range, the abundance of glycolaldehyde is increased by $2.0 \pm 0.2 \times 10^{14}$ molecules. The above evidence once again suggest that during the warm up phase, trapped radicals diffuse and exhibit additional thermal chemistry and resulting in the formation of additional glycolaldehyde molecules. The fractional abundance $f(CH_3OH)$ of glycolaldehyde at 110 K is $1.9 \pm 0.2 \times 10^{-2}$ (1.9 ± 0.2 %). After the phase change of methanol ices, the abundance of glycolaldehyde continually decreased until 150 K ($6.3 \pm 0.6 \times 10^{14}$ molecules; $f(CH_3OH) = 5.7 \pm 0.6 \times 10^{-3}$ (0.57 ± 0.06 %) possibly due to the effect of methanol sublimation and then started decreasing slowly until 180 K to an abundance of $5.0 \pm 0.5 \times 10^{14}$ molecules most likely subliming in to the gas phase. After that, the band declines quickly and finally becomes untraceable beyond 195 K.

Correlation of FTIR and ReTOF Data

Finally we would like to discuss the sublimation of glycolaldehyde monitored via online and in situ infrared spectroscopy and ReTOF mass spectroscopy. Figure S12 depicts a comparison of the infrared absorption band at 1743 cm^{-1}, assigned to glycolaldehyde, as a function of temperature with the derived sublimation profile at m/z = 60 amu recorded using ReTOF mass spectrometry in both irradiated methanol and methanol-carbon monoxide ices. In the case of irradiated methanol ices, an initial decrease of the infrared absorption at 110 K does not produce any ReTOF ion signal at m/z = 60 amu ($C_2H_4O_2$; glycolaldehyde). The decrease in apparent amount of glycolaldehyde is most likely an effect of the surrounding methanol matrix. Further evidence of this is displayed in the decrease of infrared absorption until 150 K which also did not show corresponding signal of glycolaldehyde in the gas phase. It should mention here that, isomers with molecular formula C_3H_6O, most probably propanal (CH_3CH_2CHO, I.E. 9.96 eV) or acetone (CH_3COCH_3, I.E. = 9.70 eV) were observed in the ReTOF mass spectra which started subliming at 120 K. Note that, propanal can also contribute to 1743 cm^{-1} absorption features.[14] However, the ReTOF sublimation profile of C_3H_6O isomers shows a small peak at 120 K and cannot alone explain the decrease in the infrared absorption at 1743 cm^{-1}. Further, the ReTOF sublimation profile at 150 K correlates nicely to the decrease in infrared absorption implying the sublimation of glycolaldehyde into the gas phase. Note that, infrared absorption at 1743 cm^{-1} declines completely at 175 K. As such, any ReTOF signal beyond 175 K cannot be explained by the sublimation of glycolaldehyde. Here, we are attributing signal to ethene-1,2-diol along with fragmentation of higher mass organics, such as glycerol to be the major contributor of ReTOF signal above 175 K.

In the case of irradiated methanol-carbon monoxide ices, the infrared absorption at 1743 cm^{-1} shows a sharp rise at 110 K which corresponds to the methanol phase change as discussed earlier. After the phase change of methanol ices, the 1743 cm^{-1} absorption shows a sharp decrease until 150 K correlated with methanol sublimation. As there was no observable ReTOF ion signal of glycolaldehyde at this temperature range, a matrix phase dependence on the infrared absorption value of glycolaldehyde could be present explain the apparent decrease once methanol sublimates. However, the ν_{14} band of glycolaldehyde started decreasing slowly until 180 K whereupon a rapid decline was observed. To summarize, the ReTOF sublimation profile at m/z = 60 amu, displayed signal above the noise limit at 150 K rapidly increased at 180 K; correlating

with the observed simultaneous decrease in integrated IR absorption band area of ν_{14} attributed to glycolaldehyde confirms the sublimation of this molecule.

Formation Pathways of Glycolaldehyde

Implications Based on Infrared Data

For the sake of clarity here, we would like briefly reiterate the experimental findings of the *in situ* FTIR observations pertaining to glycolaldehyde immediately following the isothermal irradiation at 5.5 K and during warm up. Recall that the glycolaldehyde was assigned based primarily on the ν_{14} band observed at 1743 cm^{-1} following deconvolution of the broad carbonyl functional absorption band, in irradiated pure amorphous methanol ice and mixed methanol carbon monoxide ice. Also note, the assignment of the molecule was further verified from the observed frequency shifts of the irradiated isotopologues. Here, in ices consisting of only *one* isotope, only *one* frequency shift of the corresponding glycolaldehyde isotopologues was observed. However, in the irradiated mixed isotopically labeled ices with *two* different atomic isotopes, e.g. $^{12}C/^{13}C$, *two* different frequencies of the ν_{14} band of glycolaldehyde were observed implying glycolaldehyde with two isotopic carbonyl units, HCO and $H^{13}CO$, are formed (see Table 3). These observations alone suggest at least two different reaction pathways leading to the synthesis of glycolaldehyde at 5.5 K and are summarized in Figure 4 (main text). Here, the carbonyl unit (HCO) can be formed either through decomposition of methanol or via hydrogenation of carbon monoxide. It should be mentioned here that, along with the first identification of glycolaldehyde, Bennett et al. proposed that the formation of this molecule proceeds by means of barrier less recombination of neighboring hydroxymethyl (CH_2OH) radical and formyl (HCO) radical formed *in situ* during exposure to ionizing radiation.[10, 13] In pure methanol ices, both of these radicals can only be formed via the radiation induced decomposition of methanol molecules. However, in the mixed methanol-carbon monoxide ices, as shown in Figure 4, CH_2OH radical can be formed either via decomposition of methanol and/or successive hydrogenation of carbon monoxide. In addition, the carbonyl unit (HCO) can be formed either via the decomposition of methanol molecule or via hydrogenation of carbon monoxide. Accordingly, presence of these radicals within the matrix results in four possible radical-radical recombination pathways to the formation of glycolaldehyde, as summarized in Figure 4. In the case of isotopically pure ices, all possibilities naturally lead to the formation of isotopically pure glycolaldehyde, hence only the observation of one carbonyl stretching band (Table 2, Figure 3B).

However, in the mixed isotopic ices, despite the possibility of four possible isotopomers of glycolaldehyde, only two isotopic carbonyl functional units are present. This, consequently, results in the detection of two different carbonyl absorption bands in the infrared absorption spectra (Figure 3B). Unfortunately, the other isotopes combinations inevitably result in the alcohol stretching of glycolaldehyde are consequently masked within the broad methanol band.

Implications Based on TPD ReTOF Mass Spectroscopy

Let us now focus attention on evidence for the formation pathways derived from the collected ReTOF sublimation profiles. In the case of irradiated mixed isotopic systems, for example the $^{13}CH_3OH$-CO system, two different radical units relevant to the synthesis of glycolaldehyde can be formed, $H^{12}CO$ / $H^{13}CO$, $^{12}CH_2CO$/$^{13}CH_2CO$, $^{12}CHOH$/$^{13}CHOH$, where units with ^{13}C isotope can be formally produced via radiolysis of methanol and ^{12}C unit can be derived via hydrogenation of carbon monoxide unit (Table 6, Figure 4). From here, four different isotopologues of glycolaldehyde can be formulated via radical-radical addition of CH_2CO with HCO unit, forming $HOCH_2CHO$ (m/z = 60 amu), $HO^{13}CH_2CHO$ (m/z = 61 amu), $HOCH_2{}^{13}CHO$ (m/z = 61 amu) and $HO^{13}CH_2{}^{13}CHO$ (m/z = 62 amu) molecules. Similarly, three possibly isotopomers of ethene-1,2-diol can be also be formulated via addition of two CHOH unit forming HOCH=CHOH (m/z = 60 amu), HOCH=^{13}CHOH (m/z = 61 amu), $HO^{13}CH=^{13}CHOH$ (m/z = 62 amu) molecules. Based on the isotope distribution in these molecules, we can thus assign m/z = 61 amu as the product from one methanol and one carbon monoxide building block, m/z = 62 amu originating from two methanol building blocks, and m/z = 60 amu from two carbon monoxide building blocks. The m/z ratios corresponding to $C_2H_4O_2$ isotopologues which can be achieved by these combinations are shown in Figure 10.

As expected, we observed ReTOF ion signal for at m/z = 61 amu (one methanol and one carbon monoxide building block) ($C^{13}CH_4O_2$, $^{13}CH_3OH$-CO system), 62 amu ($C_2H_4O^{18}O^+$, $CH_3{}^{18}OH$-CO system), 65 amu ($C^{13}CD_4O_2{}^+$, CD_3OD-^{13}CO system) and 62 amu ($C_2H_4O^{18}O^+$, CH_3OH-$C^{18}O$ system) as shown in Figure 10 (left hand side). Note that, except ion signal at m/z = 62 amu ($C_2H_4O^{18}O^+$) in CH_3OH-$C^{18}O$ system, all other masses show nearly identical sublimation profiles with two distinct peaks at 178 ± 2 K and 218 ± 2 K implying the detection of both glycolaldehyde and ethene-1,2-diol. Note that, at m/z = 62 amu ($C_2H_4O^{18}O^+$) in CH_3OH-$C^{18}O$ system, isotopomer of ethylene glycol ($HOCH_2CH_2{}^{18}OH$; Figure S14), have identical

masses and the sublimation profile has a major contribution from it which resulted in a different sublimation profile.

Further, Figure 10 also depicts the sublimation profiles of $C_2H_4O_2$ isotopologues observed at m/z = 62 amu ($^{13}C_2H_4O_2^+$) in $^{13}CH_3OH$-CO system, m/z = 64 amu ($C_2H_4{}^{18}O_2^+$) in $CH_3{}^{18}OH$-CO system, m/z = 64 amu ($C_2D_4O_2^+$) in CD_3OD-^{13}CO system and m/z = 60 amu ($C_2H_4O_2^+$) in CH_3OH-$C^{18}O$ system where these products can be formally achieved via two methanol building blocks. In the case of CD_3OD-^{13}CO ices and CH_3OH-$C^{18}O$ ices the mass-to-charges at 64 amu ($C_2D_4O_2^+$) and 60 amu ($C_2H_4O_2^+$) show similar sublimation profiles as observed in the case of m/z = 60 amu in CH_3OH-CO system. The above facts confirm the formation of both glycolaldehyde and ethene-1,2-diol involving two methanol building blocks (Table 6). Further, at m/z = 64 amu ($C_2H_4{}^{18}O_2$) in $CH_3{}^{18}OH$-CO system, the ReTOF ion signal cannot be separated from $C_2H_6O^{18}O$ (isotopomer of ethylene glycol). As in the case of $^{13}CH_3OH$-CO system, the sublimation profile suggest predominant contribution from $C^{13}CH_5O_2$ compared to $^{13}C_2H_4O_2$ at m/z = 62 amu.

Finally, $C_2H_4O_2$ isotopologues via two carbon monoxide building blocks are expected to observe at m/z = 60 amu ($C_2H_4O_2^+$) in $^{13}CH_3OH$-CO system, m/z = 60 amu ($C_2H_4O_2^+$) in $CH_3{}^{18}OH$-CO system, m/z = 66 amu ($^{13}C_2D_4O_2^+$) in CD_3OD-^{13}CO system and m/z = 64 amu ($C_2H_4{}^{18}O_2^+$) in CH_3OH-$C^{18}O$ system. In the case of $^{13}CH_3OH$-CO ices and $CH_3{}^{18}OH$-CO ices the mass-to-charges at 60 amu ($C_2H_4O_2^+$) display similar sublimation profiles as observed in the case of $C_2H_4O_2$ isomers in CH_3OH-CO system implying the formation of both glycolaldehyde and ethene-1,2-diol (Table 6). Further, at m/z = 66 amu in CD_3OD-^{13}CO system and m/z = 64 amu in CH_3OH-$C^{18}O$ system, major contributions are from $C_2D_5O_2^+$ compared to $^{13}C_2D_4O_2^+$ and $C_2H_6O^{18}O^+$ compared to $C_2H_4{}^{18}O_2^+$, respectively, are observed.

Astrophysical Relevance

Methanol and carbon dioxide have long been identified as key molecules within the interstellar medium in addition to ever abundant water and minor, yet significant constituents of

methane, ammonia and carbon dioxide.[15-20] Specifically methanol has been observed in the icy mantles in 20 out of 23 young stellar objects (YSO) observed exploiting the Infrared Space Observatory (ISO).[17] Further, some of the infrared sources such as W33 A and RAFGL 7009S, contain a significant amount of methanol in abundances up to 15% and 30%, respectively, relative to water.[21] However, most of the observed infrared sources, including several low mass star-forming regions or dark molecular clouds, methanol is found to be a minor constituent, usually with abundances at 5% or less relative to water.[17] The fluctuating abundances of methanol is well summarized in an investigation by Pontoppidan et al. (2003), where of the 40 low-mass protostars observed, only three sources displayed high (15%–25%) methanol abundances.[22]

Regarding the formation of methanol, of the first proposed mechanisms was a that of a radiative association between CH_3^+ and H_2O resulting in protonated methanol that subsequently dissociates to produce methanol.[23] From here, methanol can act as a precursor in ion-molecule reaction network chains, leading to species such as dimethyl ether and methyl formate. However, this gas phase synthetic route has been demonstrated to be drastically inefficient at forming the primary starting material, i.e. methanol, and thus consequently fails to explain the observed column densities of secondary products.[24, 25] An alternative route in methanol formation is through consecutive hydrogenation of solid state carbon monoxide via $CO \rightarrow HCO \rightarrow H_2CO \rightarrow CH_3OH$. Indeed laboratory experiments and theoretical models suggest that CH_3OH is primarily formed in the ice via this mechanism and must occur during the cold pre-stellar phase.[26-29] Further, Gibb et al reported that carbon monoxide (~ 20% with respect to H_2O abundances) is present in each young stellar object (YSO) where methanol is detected (~ 5% of methanol with respect to H_2O abundances).[17] These results support the notion that CH_3OH is probably formed in the through continual hydrogenation of carbon monoxide and thus is present in a CO-rich matrix of an icy grain mantle during most of its lifetime. Consequently, examining the induced chemical modifications of methanol and mixed methanol-carbon monoxide ices exposed to ionizing radiation is important to ultimately understanding the evolution of a molecular cloud.

Though, laboratory experiments on the energetic processing of methanol ices have been studied the past several decades (see Table S1), experiments investigating the interaction of ionizing radiation with binary mixtures of methanol and carbon monoxide are lacking; surprisingly

considering that observational data in conjunction with laboratory work implicate a methanol – carbon monoxide rich mantle of interstellar icy grains. After the first detection of glycolaldehyde in the galactic center,[30] a resurgence in methanol irradiation experiments occurred in hopes of possibly explaining the origin of this simplest sugar and it's isomers, methyl formate and acetic acid. Glycolaldehyde was first identified as product in methanol and binary mixtures of methanol carbon monoxide ices ice exposed to 5 keV electrons[10,13] and very recently in irradiated methanol ices utilizing soft X-rays.[31] However in subsequent experiments, glycolaldehyde only very briefly mentioned as an endogenous synthesized product upon exposure to ionizing radiation.[32,33]

Despite glycolaldehyde being important molecule from the perspective as an evolutionary tracer of molecular clouds to significant astrobiological implications, the formation mechanism is still somewhat disputed in the literature. Recently, Woods and corresponding authors examined the formation glycolaldehyde in dense molecular cores.[24, 25] The authors first took into consideration the proposed mechanisms in the literature (both experimental and theoretical), and concluded that the endogenous synthesis of glycolaldehyde via exposure to ionizing radiation followed with subsequent sublimation via grain warm up through star formation cannot explain the observed column densities, even if the ionizing field was increased by several orders of magnitude.[25] Instead, the authors found that a modified adaptation of a reaction scheme originally proposed by Beltran et al.,[34] can reproduce similar fractional abundances observed for glycolaldehyde. However, this modified scheme required the reaction of H_3CO (formed from the hydrogenation of formaldehyde (H_2CO)) to react with HCO, ultimately producing glycolaldehyde $HOCH_2CHO$.[35] Very recently the authors found an alternative route involving only the HCO radical; two formyl (HCO) radicals (formed from the hydrogenation of CO via grain surface chemistry) can dimerize to form HOCCOH via a barrier less reaction which can then undergo subsequent hydrogenation (+2H), ultimately producing glycolaldehyde.[24] The authors noted, that the reaction scheme was so efficient (according to their theoretical model) that only a small percentage (~0.1%) of CO needed to be hydrogenated to the formyl radical (HCO) in order to explain the observed fractional abundance of glycolaldehyde. If HCO dimerization is indeed, a favorable chemical route, then the chemical processing via the ionizing radiation field cannot inherently be dismissed as this radical has been demonstrated (with majority consensus) to be formed in methanol and methanol-carbon dioxide ices exposed to ionizing radiation.[10, 13, 32, 33] The

proposed reaction pathways of Woods et al. mainly focus on the grain-surface formation routes, suggesting the most favored pathway to be dimerization of HCO followed by hydrogenation, ultimately producing glycolaldehyde. However, previous experiments utilizing thermal hydrogen atom bombardment on a carbon monoxide ice did not yield any evidence of glycolaldehyde,[26, 36-39] strongly indicating that the HCO dimerization is not as efficient as predicted. However, reactions of the CH_2OH and HCO radicals, synthesized via exposure to ionizing radiation in the bulk ices followed with warm up phase of a molecular cloud is still relevant to the astrophysical formation of glycolaldehyde as demonstrated in this experimental investigation.

Most of the previous experiments listed in Table S1, comprised of identifying chemical changes mainly via infrared spectroscopy. Unfortunately, relying only on this technique can lead to ambiguous assignments of *complex* organics (which may have been formed through energetic processing) due to the overlapping of similar group frequencies. Recently, utilizing single photon reflectron time-of-flight (ReTOF) mass spectrometry in addition to solid state FTIR spectroscopy, our group has made a crucial progress toward a detailed understanding of several key classes of complex organic molecules[14, 40] specifically saturated and unsaturated aldehydes/ketones, saturated and unsaturated dicarbonyls (aldehydes/ketones), saturated tricarbonyls (aldehydes/ketones) as well as molecules containing both carbonyl and alcohol functional groups and fully saturated alcohols and diols formed in the radiation-induced processing of simple binary ices of methane and carbon monoxide. Further, in irradiated amorphous methane ices, hydrocarbons of alkanes, alkenes, and alkynes/dienes as large as $C_{22}H_{2n+2}$ have been elucidated utilizing ReTOF mass spectroscopy.[40] The continued success of the single photon TPD ReTOF mass spectrometry approach in identifying astrochemically relevant complex organics synthesized in simple ices of methanol and methanol-carbon monoxide has again been demonstrated here.

Here, two complementary detection techniques, FTIR spectroscopy and single photoionization ReTOF mass spectrometry were employed to analyze the endogenous synthesized products formed via radiation induced chemical processing. These coupled techniques confirm the detection glycolaldehyde in irradiated ices of methanol and methanol-carbon monoxide ices both in the solid stated and warm-up phase. In the irradiated methanol ices, a maximum of $8.0 \pm 0.8 \times 10^{14}$ molecules (70 K) and minimum of $3.2 \pm 0.8 \times 10^{14}$ molecules (150 K) of glycolaldehyde were produced with a fraction of $4.5 \pm 0.5 \times 10^{-3}$ and $1.8 \pm 0.2 \times 10^{-3}$ with

respect to the initial amount of methanol. Following a procedure in estimating an upper limit on the fractional abundances for methyl formate formed in the irradiation of methanol-carbon monoxide ices as presented by Modica et al.,[32] we estimate that the fractional abundances of glycolaldehyde formed in the ices is within $4.5 \pm 0.5 \times 10^{-8}$ and $1.8 \pm 0.2 \times 10^{-8}$ with respect to H_2 abundances. Further, in the case of methanol-carbon monoxide ices, the energetic processing followed by subsequent warm-up resulted detection of a maximum of $2.1 \pm 0.2 \times 10^{15}$ molecules (110 K) and minimum of $6.3 \pm 0.2 \times 10^{14}$ (150 K) molecules of glycolaldehyde molecules are formed within fractions of $1.9 \pm 0.2 \times 10^{-2}$ and $5.7 \pm 0.6 \times 10^{-3}$ with respect to total number of methanol molecules deposited initially. This leads to an estimated fractional abundances of glycolaldehyde formed in these experiments at $1.9 \pm 0.2 \times 10^{-7}$ and $5.7 \pm 0.6 \times 10^{-8}$ with respect to molecular hydrogen. These glycolaldehyde abundances are close to the estimated abundances towards the hot core G31.40+0.31 (~5×10^{-8} relative to H_2),[41] and towards IRAS 16293-2422 (~5×10^{-9} relative to H_2).[42] Our estimated abundances are almost three order of magnitude larger than the estimated abundances of glycolaldehyde in Sgr B2 (N) (~5.9×10^{-11} relative to H_2), which can possibly be attributed to lower abundances of methanol in Sgr B2 (N) (4×10^{-8} with respect of H_2).[43]

As previously stated, the formation routes of glycolaldehyde in methanol ices via recombination of HCO and CH_2OH radicals (formed in the bulk ice upon exposure to ionizing radiation) has been suggest to inefficient and consequently cannot reproduce the observed abundances of glycolaldehyde via grain surface chemistry in the dense core condition.[24, 25] This is highly disputed, and our laboratory experiments do not support this conclusion at all. However, the estimated fractional abundances in the present experiment with methanol ices are close to the reported values towards the hot core G31.40+0.31,[41] and IRAS 16293-2422 and hence these reaction pathways prove relevant in the chemical modification via exposure to ionizing radiation in the bulk phase.[10, 25] Further, formation of glycolaldehyde increases almost five times in binary ices of methanol and carbon monoxide suggesting the reaction pathway of hydrogenation of carbon monoxide to be a major contributor in the formation of glycolaldehyde.

In the mixed isotopic ices of methanol and carbon monoxide, infrared FTIR studies suggests the formation of at least two different carbonyl unit (HCO) reaction pathways via radiolysis and subsequent decomposition of methanol in addition to hydrogenation of carbon

monoxide molecules (Figure 3B and Table 2) are relevant to the formation of glycolaldehyde. Accordingly, during the TPD studies of these ices using single photoionization ReTOF mass spectrometry, we were able to detect glycolaldehyde at three different isotopic masses, suggesting at least three competing reaction mechanisms involved in the formation of glycolaldehyde in the irradiated ices; (i) formation of glycolaldehyde via hydrogenation mechanism of carbon monoxide as proposed by Charnley and Rodgers,[25, 44] (ii) formation of glycolaldehyde via the reaction one methanol unit to carbon monoxide unit and (iii) via decomposition of methanol molecule followed by recombination of HCO and CH_2OH radicals.[10, 13, 25] In conclusion, this study presents conclusive evidence on the formation of glycolaldehyde *inside bulk ices involving non-equilibrium chemistry* ultimately revealing that fractional abundances of glycolaldehyde, similar to observation, are capable of being produced within ices of methanol and mixtures of methanol-carbon monoxide with energetic doses relevant to the typical lifetime ($\sim 10^5$-10^6 years) of an interstellar grain prior to the star forming induced warm up phase.[45, 46]

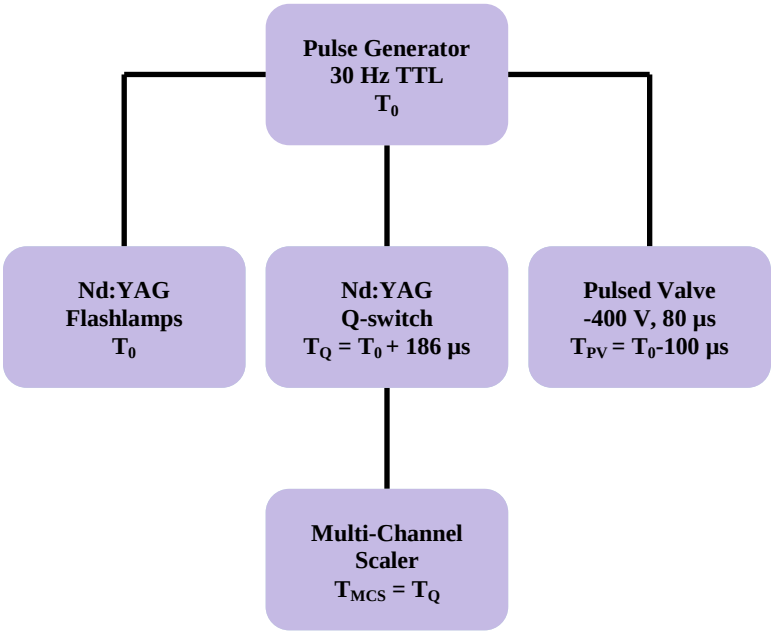

Figure S1. Pulse sequence of the single photoionization reflectron time-of-flight mass spectrometer relative to the time zero starting pulse (T_0) operating at 30 Hz. The start trigger of the multichannel scaler is synched to the Q-switch of the laser system, while the pulse valve has been optimized to open 100 µs prior to T_0.

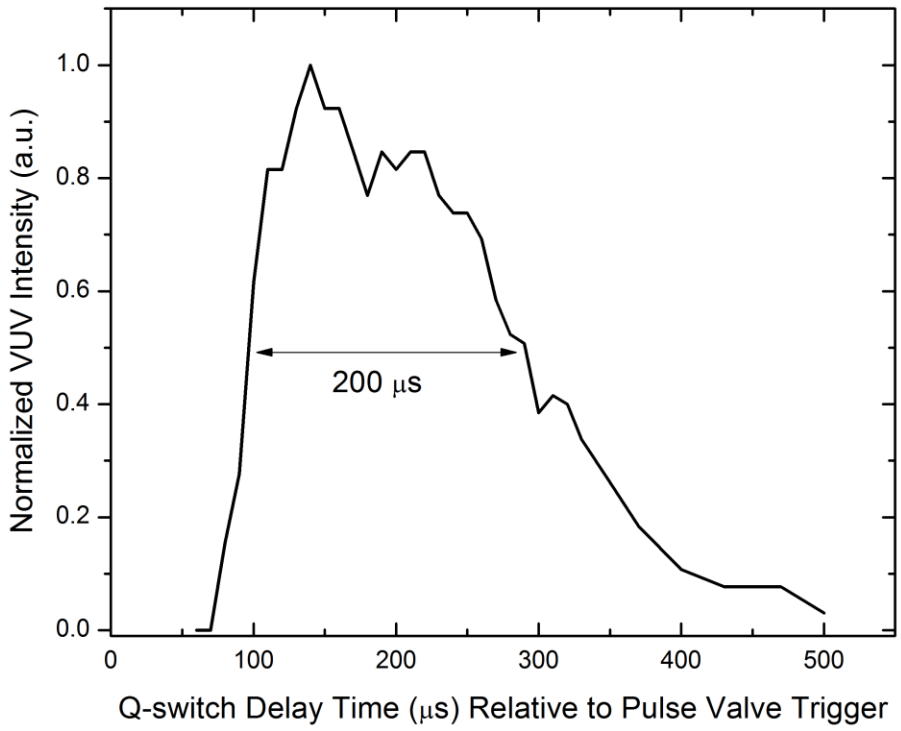

Figure S2. Normalized VUV intensity plotted as a function of the delay time between the pulse valve trigger and laser Q-switch operating at constant ω_{UV} energy (20 mJ per pulse) and xenon backing pressure of 2.7 atm. The VUV intensity reflects the overall pulse shape of the piezoelectric valve.

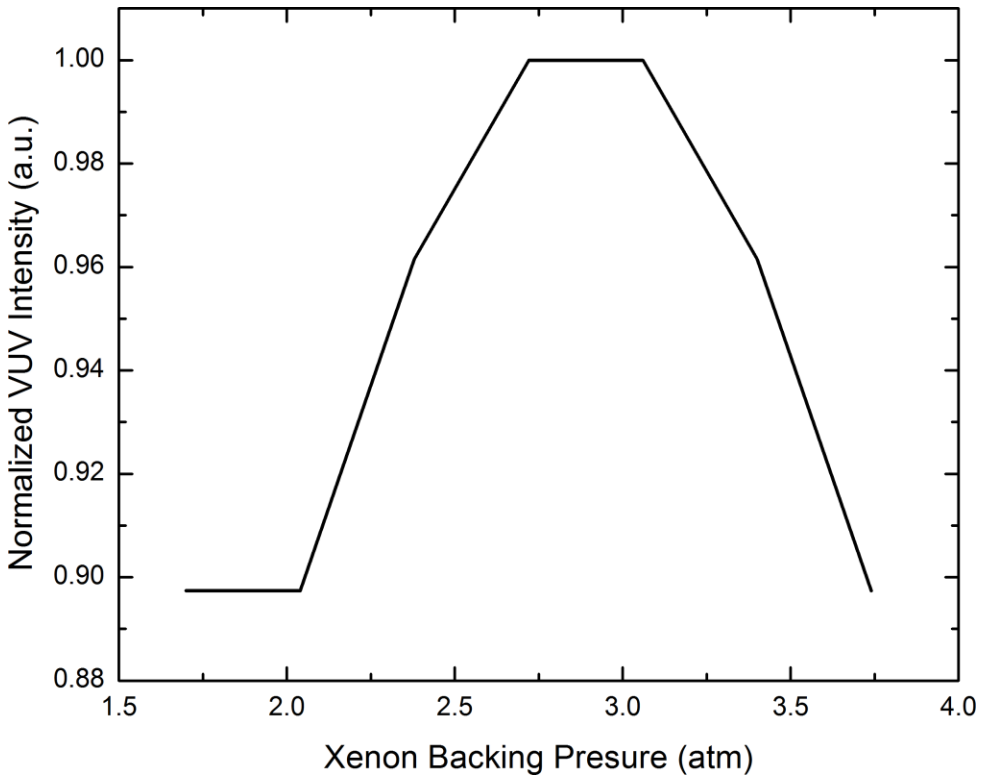

Figure S3. Normalized VUV intensity as a function of xenon backing pressure with a constant ω_{UV} energy of 27 mJ per pulse. The decrease after 3 atm is caused by self- attenuation of the noble gas.

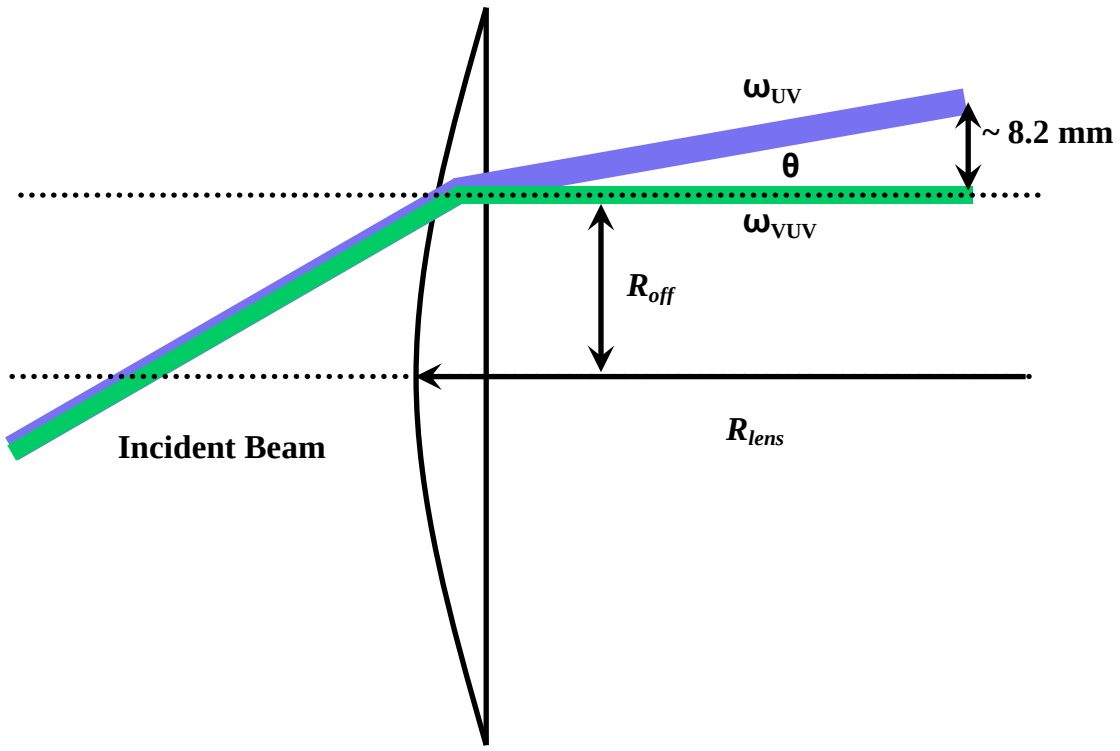

Figure S4. Schematic representation of the separation of the two collinear ω_{UV} (blue) and ω_{VUV} (green) beams utilizing an off axis planoconvex lithium fluoride (LiF) lens. The geometry of the experimental setup allows for a separation of approximately 8.2 mm between the two beams. See text for details describing the angle of separation (θ) and associated constants; the figure is not drawn to scale for clarity.

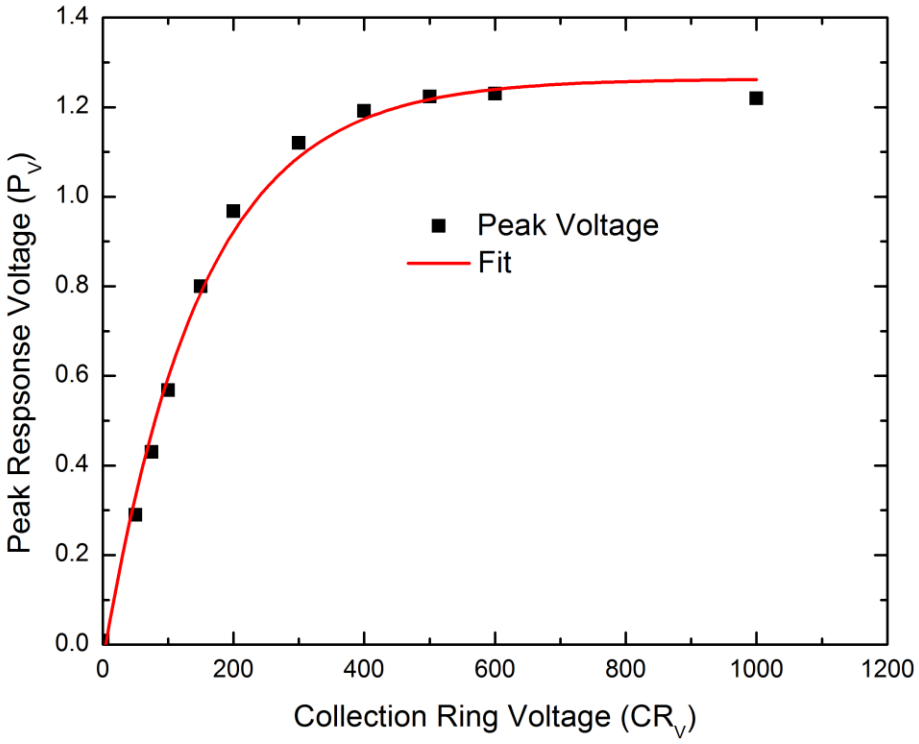

Figure S5. The VUV photoelectric detector response as a function of voltage applied to the collection ring was plotted along with the fit (solid line). The error bars are in the same order of magnitude of the dimension of the square.

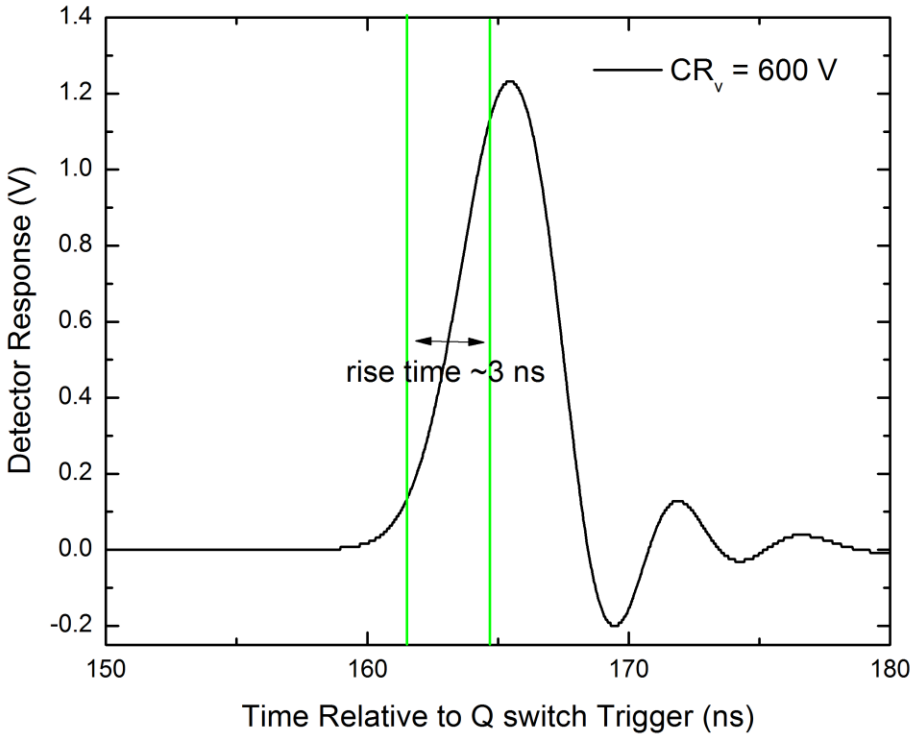

Figure S6. Realtime response of the VUV photoelectron detector with an applied voltage of 600 V to the collection ring (saturation level). The rise time is approximately 3 ns as defined as the time between 10% of the baseline value and 90% of the peak with a pulse width (FWHM) of 4 ns. The oscillations at the end are caused by a slight impedance mismatch.

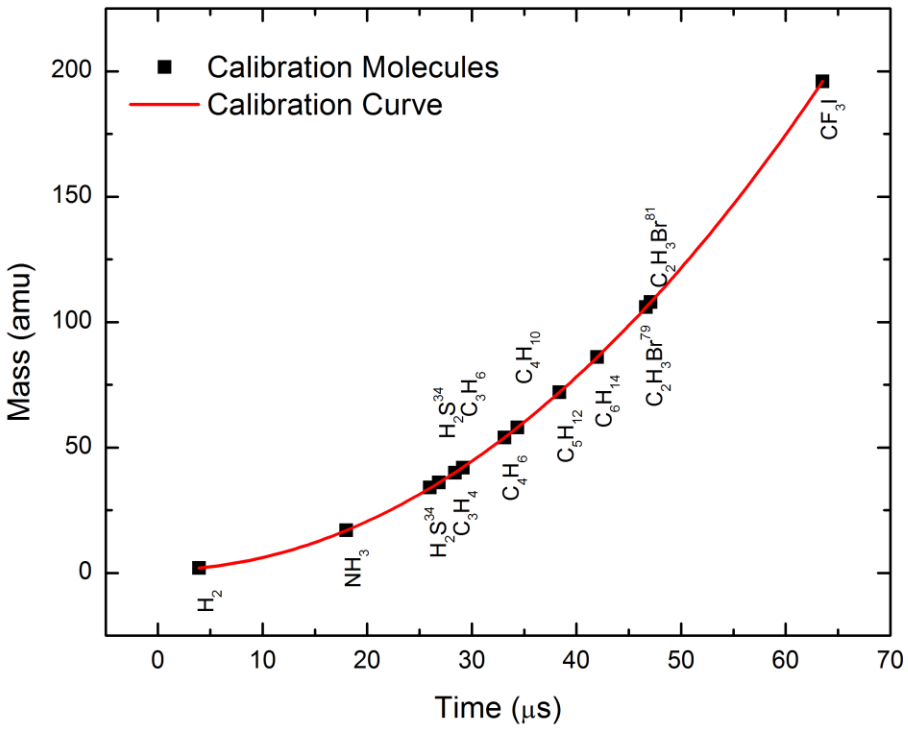

Figure S7. Calibration curve of the ReTOF mass spectra using ammonia (NH_3), hydrogen sulfide (H_2S), allene (C_3H_4), propene (C_3H_6), 1,3-butadiene (C_4H_6), n-butane (C_4H_{10}), n-pentane (C_5H_{12}), n-hexane (C_6H_{14}), vinyl bromide (C_2H_3Br), and iodotrifluoromethane (CF_3I) as well as their isotopologues. The best fit curve was achieved by a 3rd degree polynomial.

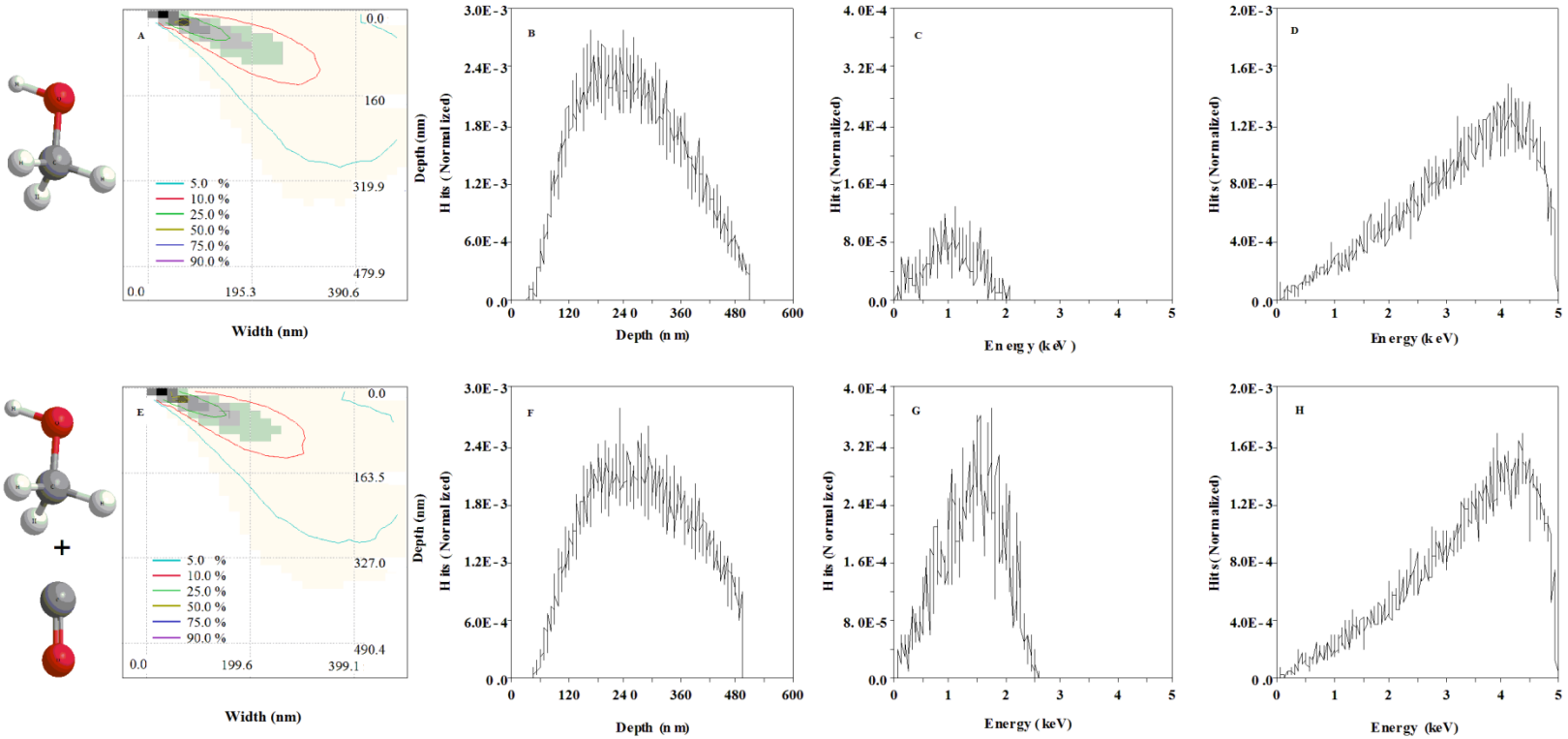

Figure S8. CASINO simulation results of electron trajectories for methanol (CH_3OH) (top) and methanol-carbon monoxide (CH_3OH-CO) ices (bottom): (A, E) Absorbed energy; (B, F) Penetration depth of the electrons into the ice; (C, G) Energy of the transmitted electrons; (D, H) Backscattered energy (BSE) of the electrons.

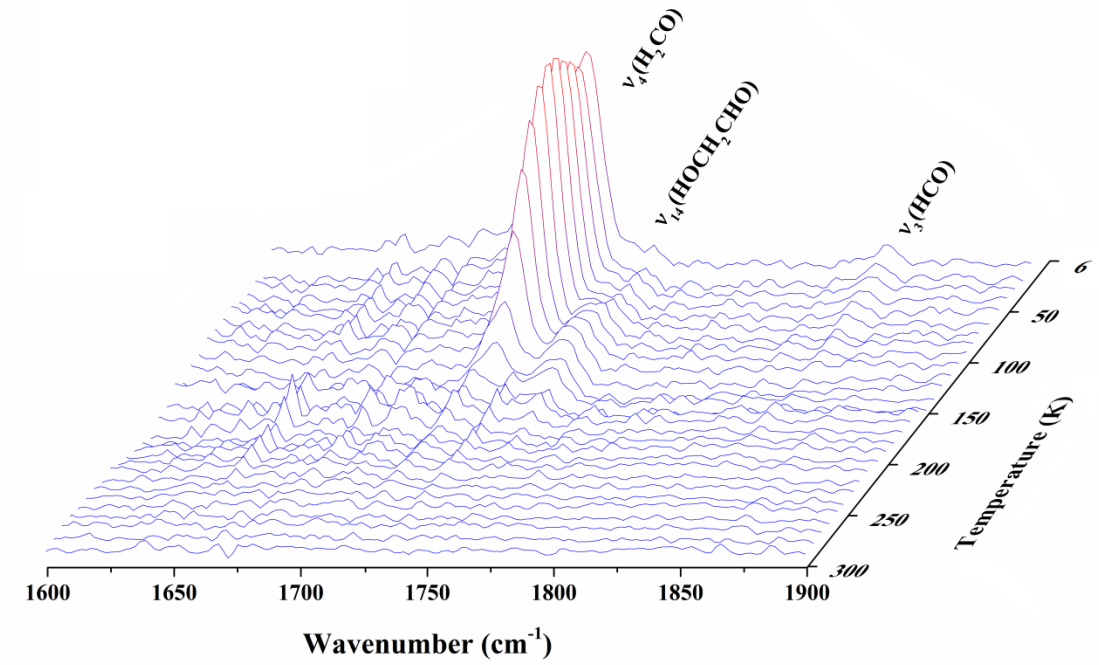

Figure S9. Infrared absorption spectra in 1900-1600 cm^{-1} region as a function of temperature in irradiated methanol (CH_3OH) ices during warm-up phase. Here, an inverted frequency axis is presented to clearly show the temporal change of the glycolaldehyde absorption feature. The ν_{14} band of methyl formate is hidden within the shoulder of formaldehyde (ν_4).

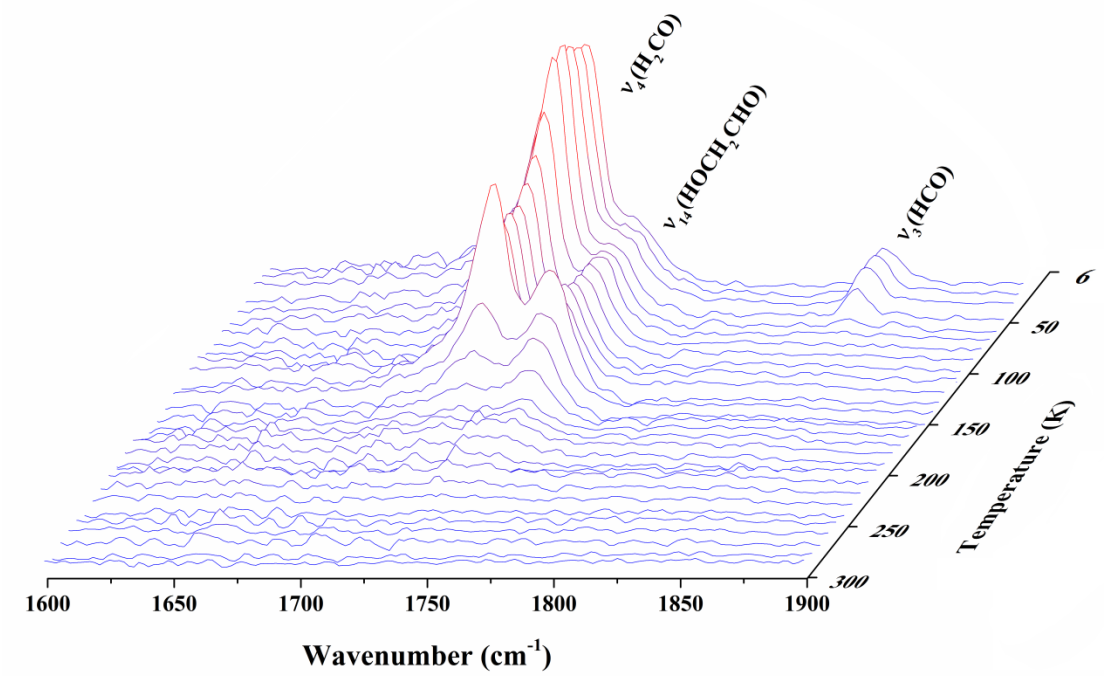

Figure S10. Infrared absorption spectra in 1900-1600 cm^{-1} region as a function of temperature in irradiated methanol-carbon monoxide (CH_3OH-CO) ices during warm-up phase. Here, an inverted frequency axis is presented to clearly show the temporal change of the glycolaldehyde absorption feature. The ν_{14} band of methyl formate is hidden within the shoulder of formaldehyde (ν_4).

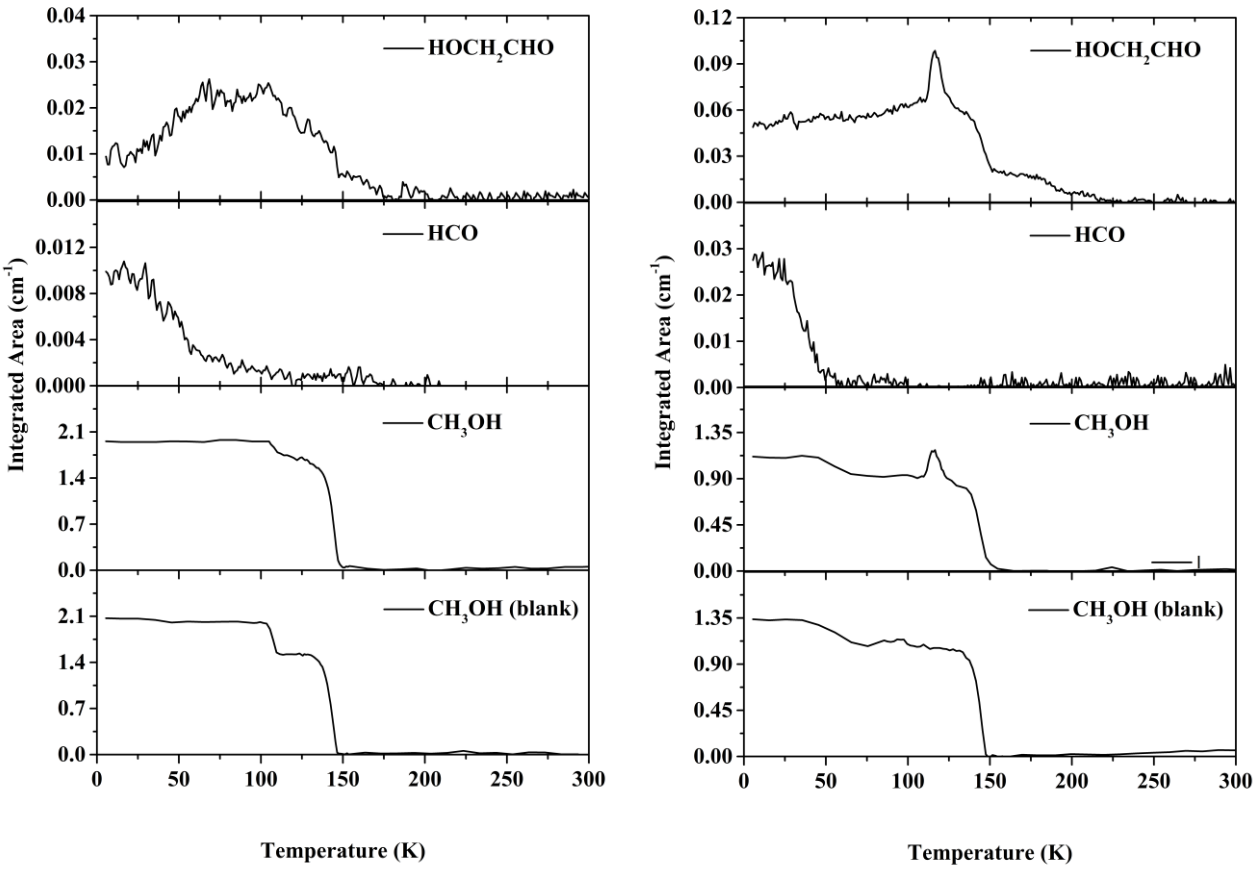

Figure S11. (Left) Temporal profiles of glycolaldehyde ($HOCH_2CHO$ at 1743 cm^{-1}), of the formyl radical (HCO at 1842 cm^{-1}), and of methanol (CH_3OH at 1028 cm^{-1}) during the warm-up period of the irradiated methanol ices. (Right) Temporal profiles of glycolaldehyde ($HOCH_2CHO$ at 1743 cm^{-1}), of the formyl radical (HCO at 1842 cm^{-1}), and of methanol (CH_3OH at 1028 cm^{-1}) during the warm-up period of irradiated methanol-carbon monoxide ices. In case of methanol-carbon monoxide ices, the pronounced peaks observed at 110 K are most likely due to the phase transition of the methanol matrix as reported previously.[10] Further, the unique nature of the strong peaks in methanol-carbon monoxide ices compared to pure methanol are possibly due to the more porous nature of the CH_3OH-CO ices at 110 K due the early sublimation of carbon monoxide (40 K).

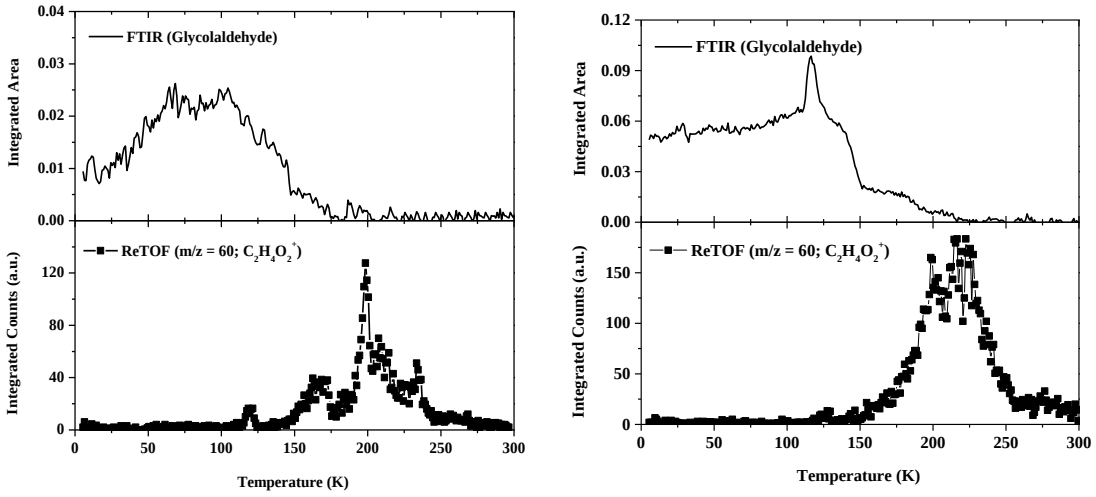

Figure S12. Top: temporal profiles of the glycolaldehyde ($HOCH_2CHO$) absorption band at 1743 cm^{-1} in irradiated methanol (left) and methanol-carbon monoxide ices (right). Bottom: sublimation profiles of $C_2H_4O_2$ (m/z = 60) isomers recorded via ReTOFMS-PI during warm-up phase of irradiated methanol (left) and methanol-carbon monoxide ices (right).

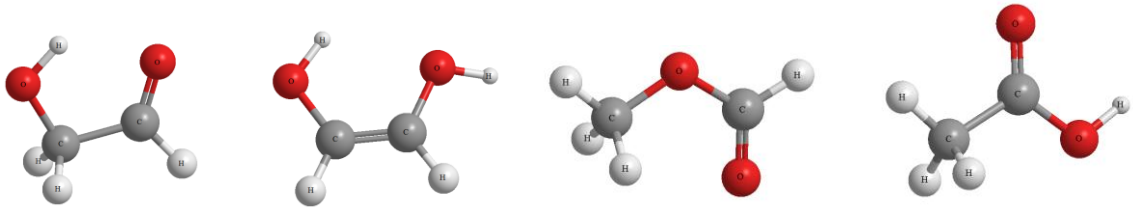

Glycolaldehyde
10.20 eV
117 ± 2 kJ mol^{-1}

Ethene-1,2-diol
9.62 eV
117 ± 2 kJ mol^{-1}

Methyl formate
10.84 eV
96 kJ mol^{-1}

Acetic acid
10.63 eV
0.0 kJ mol^{-1}

Figure S13. Four lowest energy isomers with generic molecular formula $C_2H_4O_2$ along with their ionization energies (IE) and relative enthalpies of formation (ΔH_f^0) taken from the NIST database (in case glycolaldehyde, IE from ref.[47], ΔH_f^0 from ref. [48]). Recall that the ionization laser for this experiment is operating at 10.49 eV. Consequently, glycolaldehyde and ethene-1,2-diol can be ionized in the present experimental setup.

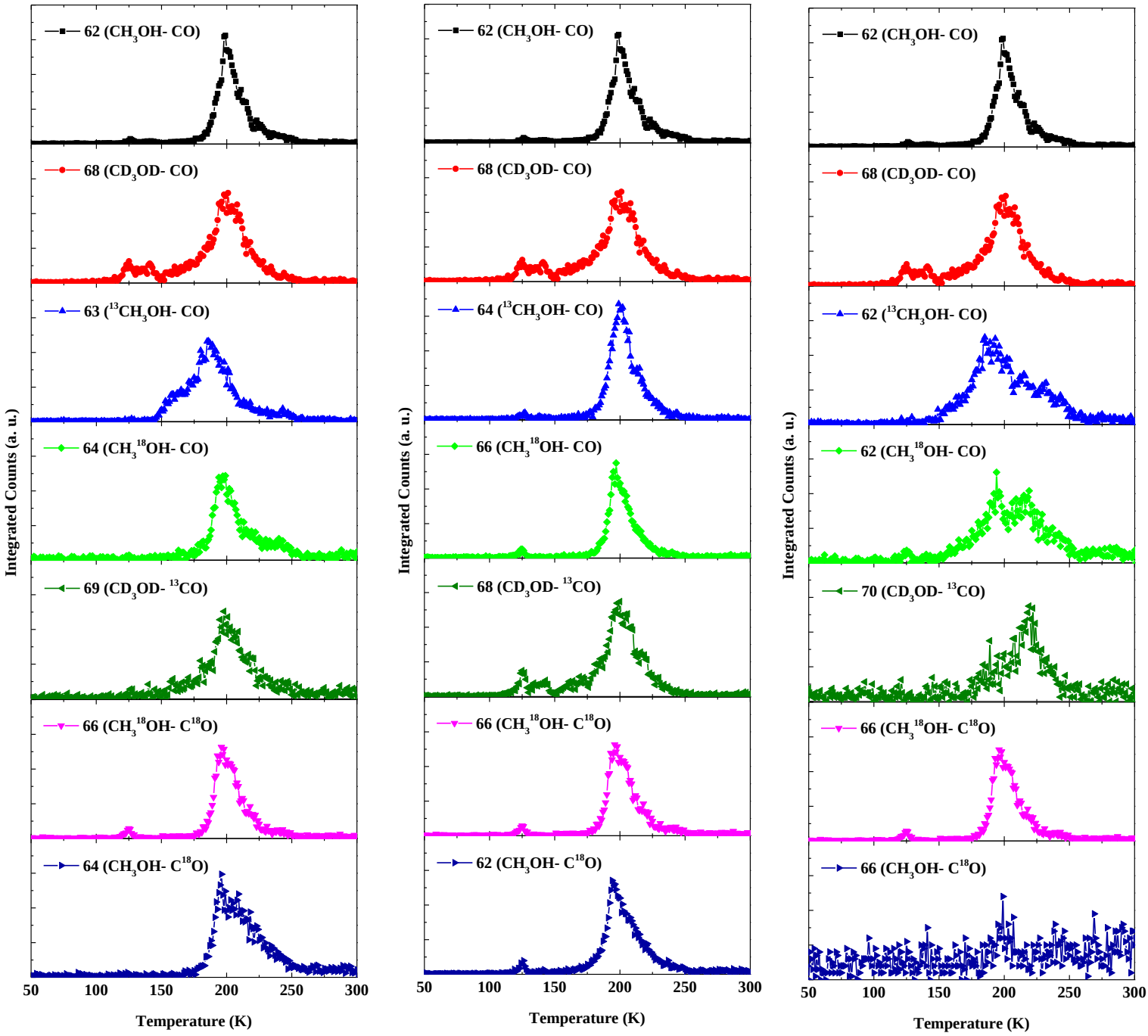

Figure S14. Sublimation profiles of $C_2H_6O_2$ isotopomers in methanol-carbon monoxide ices. The graphs in the left depict the sublimation profile of $C_2H_6O_2$ isotopologues formally derived from radicals of one methanol and one carbon monoxide building block; graphs in the middle depict the sublimation profiles of $C_2H_6O_2$ isotopologues which can only be synthesized from two methanol building blocks. The graphs in the right depict the sublimation profile of $C_2H_6O_2$ isotopologues which can be formally formed from two carbon dioxide building blocks.

Table S1. Compilation of previous experimental studies on the energetic processing of pure methanol (CH_3OH) and of methanol (CH_3OH) - carbon monoxide (CO) ices.

Ice composition	Ionizing radiation	Dose per 16 amu	Dose per molecule	Molecules identified *in situ*
CH_3OH - Ar (1:100) [49]	UV at 8.4 eV	Not Specified	–	CH_2OH
CH_3OH[50]	γ Radiation	100 eV	200 eV per CH_3OH	H_2, H_2CO, $HOCH_2CH_2OH$
CH_3OH[51]	Broad Band X-rays	Not Specified	–	CH_3, CH_3O, CH_2OH
CH_3OH[52]	3 keV He^+	60 eV	120 eV per CH_3OH	H_2O, H_2CO, CO_2, CO, CH_4, CH_3COCH_3
CH_3OH[53]	3 keV He^+	60 eV	120 eV per CH_3OH	H_2CO, CO_2, CO, CH_4, CH_3COCH_3
CH_3OH[54]	0.7 MeV H^+	0.12 eV	0.24 eV per CH_3OH	None; the paper focused on radiation induced phase change of crystalline to amorphous
CH_3OH[55]	Broad band UV	Not Specified	–	H_2CO, CO_2, CO, CH_4, HCO, H_2, $HCOOCH_3$, generic "alcohols"
CH_3OH[56]	1 MeV H^+	17 eV	34 eV per CH_3OH	CO_2, CO, HCO, CH_4, H_2CO, C_2H_5OH, CH_3COCH_3
CH_3OH[57]	3 keV He^+	52 eV	104 eV per CH_3OH	CO_2, CO, CH_4, H_2O, H_2CO, CH_3COCH_3
CH_3OH[58]	30 keV He^+	80 eV	160 eV per CH_3OH	CO, CO_2, CH_4, H_2CO
	Broad Band UV	40 eV	80 eV per CH_3OH	
CH_3OH[59]	200 keV H^+ 400 keV Ar^{2+}	350 eV	700 eV per CH_3OH	None; focused on the reflectance curve and the corresponding relationship to outer solar system icy bodies colors
CH_3OH[10]	5 keV e^-	0.7 eV	1.4 eV per CH_3OH	CO, CO_2, CH_4, H_2CO, HCO, $HOCH_2CHO$, $HCOOCH_3$

CH_3OH[18]	Broad Band UV	Not Specified	–	CO, HCO, H_2CO, CH_4, $HCOOCH_3$
CH_3OH - CO (1:1) [18]				
CH_3OH[60]	Broad Band X-rays	≤ 0.001 eV	2.3×10^{-2} to 2.8×10^{-1} eV per CH_3OH	H_2CO
CH_3OH[32]	200 keV H^+	34.2 eV	68.4 eV per CH_3OH	CO, CO_2, H_2CO, CH_4, H_2CO, HCO, $HOCH_2CHO$, $HCOOCH_3$
CH_3OH - CO (10:16) [32]		18.7 eV	20.1 eV per CO 14.4 eV per CH_3OH	
CH_3OH[61]	16 MeV O^{5+}	3.2 eV	6.3 eV per CH_3OH	CO, CO_2, H_2CO, CH_2OH, CH_4, HCO, CH_3OCHO
	220 MeV O^{7+}	1.6 eV	3.2 eV per CH_3OH	
	606 MeV Zn^{20+}	11 eV	22 eV per CH_3OH	
	774 MeV Kr^{31+}	12 eV	24 eV per CH_3OH	
CH_3OH[33]	200 keV H^+	16.2 eV	32.4 eV per CH_3OH	CH_4, CO_2, H_2CO, $HOCH_2CH_2OH$, $HCOOCH_3$, $HOCH_2CHO$
CH_3OH - CO (10:16) [33]		18 eV	19.4 eV per CO 13.8 eV per CH_3OH	
CH_3OH[31]	Broad Band X-rays (0.3-1.2 keV)	920 eV	1840 eV per CH_3OH	CH_2OH, H_2CO, CH_4, HCOOH, $HOCH_2CHO$, CH_3COOH, CH_3OCH_3, $HCOOCH_3$, $(CH_2OH)_2$, HCO, CO, CO_2
	0.3 keV X-rays	0.25 eV	0.5 eV per CH_3OH	
	0.55 keV X-rays	1.06 eV	2.1 eV per CH_3OH	

Table S2. Absorption features observed in the methanol ice before and after the irradiation.

CH_3OH		CD_3OD		$^{13}CH_3OH$		$CH_3{}^{18}OH$		Assignments	Carrier
Before[10, 62]	After	Before[62]	After	Before	After	Before	After		
4399						4398		$\nu_2/\nu_9+\nu_4/\nu_6/\nu_{10}$ (CH_3OH)	Combination
4274						4273		$\nu_2/\nu_9+\nu_4$ (CH_3OH)	Combination
4016						3989		$\nu_2/\nu_9+\nu_8$ (CH_3OH)	Combination
3987						3960		$\nu_2/\nu_9+\nu_8$ (CH_3OH)	Combination
3468,3250, 3248, 3060		2508,2428, 2336		3236		3455,3372, 3251		ν_1 (CH_3OH)	Fundamental
2990		2245		2975		2984		ν_2 (CH_3OH)	Fundamental
2958		2216		2945		2956		ν_9 (CH_3OH)	Fundamental
2918		2151		2920		2928		$\nu_4+\nu_5/\nu_4+\nu_{10}/\nu_5+\nu_{10}/2\nu_4/2\nu_{10}/2\nu_5$ (CH_3OH)	Combination / Overtone
2825		2071		2824		2825		$\nu_3/2\nu_6$ (CH_3OH)	Fundamental / Overtone
2603		2010		2610		2607		$\nu_4+\nu_{11}/\nu_7+\nu_4/\nu_6/\nu_{10}$ (CH_3OH)	Combination
2524		…		2511		2526		$\nu_6+\nu_{11}$ (CH_3OH)	Combination
2432		…		2412		2419		$\nu_6+\nu_8$ (CH_3OH)	Combination
	2339							ν_3 (CO_2)	Fundamental
2241		1938		2229		2223		$2\nu_{11}/2\nu_7$ (CH_3OH)	Overtone
	…		…		2067		2107	ν_2 (H_2CCO)	Fundamental
	2135			2087			2083	ν_1 (CO)	Fundamental
2040		1661		2004		1991		$2\nu_8$ (CH_3OH)	Overtone
	1842		1786		1797		...	ν_3 (HCO)	Fundamental
	1743		1711		1703		1713	ν_{14} ($HOCH_2CHO$)	Fundamental
	1726		1676		1687		1693	ν_4 (H_2CO)	Fundamental
	1499		…		1499		1496	ν_3 (H_2CO)	Combination
1475		1124		1475		1475		ν_4 (CH_3OH)	Fundamental
1460		1062		1458		1461	1844	ν_{10} (CH_3OH)	Fundamental
1445		1099		1440		1445	1745	ν_5 (CH_3OH)	Fundamental
1420		1062		1420		1417	1718	ν_6 (CH_3OH)	Fundamental

	1304		…		1296		1304	ν_4 (CH_4)	Fundamental
	1246		…		…		…	ν_2 (H_2CO)	
	1192		…		1167		1168	ν_4 (CH_2OH)	Fundamental
1159, 1130, 1123		900		1124, 1116		1159, 1130, 1123		ν_7 (CH_3OH)	Fundamental
	1094				928		1080	ν_9 ($HOCH_2CH_2OH$)	Fundamental
1040		979		1022		1015		ν_{11} (CH_3OH)	Fundamental
1028		831		1010		...		ν_8 (CH_3OH)	Fundamental

Table S3. Absorption features observed in the methanol – carbon monoxide ice before and after the irradiation.

CH_3OH-CO		CD_3OD-CO		$^{13}CH_3OH$-CO		$CH_3{}^{18}OH$-CO		Assignments	Carrier
Before[10, 62]	After	Before[62]	After	Before	After	Before	After		
4399				4385		4395		$\nu_2/\nu_9+\nu_4/\nu_6/\nu_{10}$ (CH_3OH)	Combination
4274				4276		4276		$\nu_2/\nu_9+\nu_4$ (CH_3OH)	Combination
4247		4246		4246		4245		$2\nu_1$ (CO)	Overtone
4021				3993		3994		$\nu_2/\nu_9+\nu_8$ (CH_3OH)	Combination
3987				3959		3960		$\nu_2/\nu_9+\nu_8$ (CH_3OH)	Combination
3623		2674		3621		3609		ν_1 (CH_3OH ··· CO)	Fundamental
3462,3383, 3271, 3123		2564,2511, 2439,2366		3464,3380, 3277,3125		3455,3372, 3251		ν_1 (CH_3OH)	Fundamental
2985		2248		2975		2984		ν_2 (CH_3OH)	Fundamental
2956		2217		2949		2956		ν_9 (CH_3OH)	Fundamental
2925		2150		2923,2906		2928		$\nu_4+\nu_5/\nu_4+\nu_{10}/\nu_5+\nu_{10}/2\nu_4/2\nu_{10}/2\nu_5$ (CH_3OH)	Combination / Overtone
2828		2073		2824		2828		$\nu_3/2\nu_6$ (CH_3OH)	Fundamental / Overtone
2604		2013		2594		2604		$\nu_4+\nu_{11}/\nu_7+\nu_4/\nu_6/\nu_{10}$ (CH_3OH)	Combination
2524		..		2511		2520		$\nu_6+\nu_{11}$ (CH_3OH)	Combination
2438		..		2419		2429		$\nu_6+\nu_8$ (CH_3OH)	Combination
	2342		2342		2341		2342	ν_3 (CO_2)	Fundamental
					2275		2324	ν_3 ($^{13}CO_2/C^{18}O_2$)	Fundamental
2226		1931		2219		2220		$2\nu_{11}/2\nu_7$ (CH_3OH)	Overtone
2135		2136		2135		2136		ν_1 (CO)	Fundamental
2089				2089		2088		ν_1 ($^{13}CO/C^{18}O$)	Fundamental
						2106		ν_2 ($H_2CC^{18}O$)	Fundamental
2047		1666		2014		1995		$2\nu_8$ (CH_3OH)	Overtone
	1842		…		1844		1844	ν_3 (HCO)	Fundamental
	1743		…		1743		1743	ν_{14} ($HOCH_2CHO$)	Fundamental
	1726		1686		1724		1724	ν_4 (H_2CO)	Fundamental
	1697		…		…		…	$2\nu_6$ ($HOCH_2CHO$)	Overtone

	1497		…		1499		1496	ν_3 (H_2CO)	Combination
1475		1124		1475		1475		ν_4 (CH_3OH)	Fundamental
1461		1063		1458		1461		ν_{10} (CH_3OH)	Fundamental
1445		1099		1444		1445		ν_5 (CH_3OH)	Fundamental
1421		1062		1420		1417		ν_6 (CH_3OH)	Fundamental
	1303		…		1298		1304	ν_4 (CH_4)	Fundamental
	1193		…		1165		1162	ν_4 (CH_2OH)	Fundamental
1153, 1129, 1117		900		1124, 1116		1159,1123, 1111		ν_7 (CH_3OH)	Fundamental
	1094		…		913		1089	ν_9 ($HOCH_2CH_2OH$)	Fundamental
	1062		…		…		…	ν_7 ($HOCH_2CHO$)	Fundamental
1039		977		1019		1011		ν_{11} (CH_3OH)	Fundamental
1028		833		…		…		ν_8 (CH_3OH)	Fundamental

Continued

CD_3OD-^{13}CO		$CH_3{}^{18}OH$-$C^{18}O$		CH_3OH-$C^{18}O$		Assignments	Carrier
Before[62]	After	Before	After	Before	After		
		4397		4403		$\nu_2/\nu_9+\nu_4/\nu_6/\nu_{10}$ (CH_3OH)	Combination
		4274		4277		$\nu_2/\nu_9+\nu_4$ (CH_3OH)	Combination
4152		4146		4145		$2\nu_1$ (CO)	Overtone
		3998		4023		$\nu_2/\nu_9+\nu_8$ (CH_3OH)	Combination
		3962		3987		$\nu_2/\nu_9+\nu_8$ (CH_3OH)	Combination
2674		3608		3620		ν_1 ($CH_3OH \cdots CO$)	Fundamental
2564,2511, 2439,2366		3455,3372, 3251		3462,3383, 3271, 3123		ν_1 (CH_3OH)	Fundamental
2248		2985		2986		ν_2 (CH_3OH)	Fundamental
2218		2952		2956		ν_9 (CH_3OH)	Fundamental
2150		2921		2925		$\nu_4+\nu_5/\nu_4+\nu_{10}/\nu_5+\nu_{10}/2\nu_4/2\nu_{10}/2\nu_5$ (CH_3OH)	Combination / Overtone
2073		2828		2828		$\nu_3/2\nu_6$ (CH_3OH)	Fundamental / Overtone

2013		2601		2601		$\nu_4 + \nu_{11}/\nu_7+\nu_4/\nu_6/\nu_{10}$ (CH_3OH)	Combination
…		2519		2524		$\nu_6+\nu_{11}$ (CH_3OH)	Combination
…		2419		2438		$\nu_6+\nu_8$ (CH_3OH)	Combination
	…		2307		2324	ν_3 (CO_2)	Fundamental
	2275				2307	ν_3 (CO_2)	Fundamental
			2107		2106	ν_2 ($H_2CC^{18}O$)	Fundamental
1932		2227		2223		$2\nu_{11}/2\nu_7$ (CH_3OH)	Overtone
2137		…		2086	2137	ν_1 (CO)	Fundamental
2088		2086				ν_1 (CO)	Fundamental
2038		2037		2037		ν_1 ($^{13}C^{18}O$)	Fundamental
1666		2001		2047		$2\nu_8$ (CH_3OH)	Overtone
	…		1799		1799	ν_3 (HCO)	Fundamental
	…		1716		…	ν_{14} ($HOCH_2CHO$)	Fundamental
	1678		1693		1726	ν_4 (H_2CO)	Fundamental
	...		…		…	$2\nu_6$ ($HOCH_2CHO$)	Overtone
…	…		1488		1497	ν_3 (H_2CO)	Combination
1124		1474		1476		ν_4 (CH_3OH)	Fundamental
1063		1458		1460		ν_{10} (CH_3OH)	Fundamental
1101		1449		1445		ν_5 (CH_3OH)	Fundamental
1062		1421		1425		ν_6 (CH_3OH)	Fundamental
	…	…	1303		1304	ν_4 (CH_4)	Fundamental
	...	**...**	...		1194	ν_4 (CH_2OH)	Fundamental
900		1125,1123		1153, 1129, 1117		ν_7 (CH_3OH)	Fundamental
	...		...		1087	ν_9 ($HOCH_2CH_2OH$)	Fundamental
	...		...		1062	ν_7 ($HOCH_2CHO$)	Fundamental
978		1010		1039		ν_{11} (CH_3OH)	Fundamental
831		**...**		…		ν_8 (CH_3OH)	Fundamental

References:

1. R. Hilbig and R. Wallenstein, *Quantum Electronics, IEEE Journal of*, 1981, **17**, 1566-1573.
2. A. H. Kung, *Opt. Lett.*, 1983, **8**, 24-26.
3. R. Mahon, T. McIlrath, V. Myerscough and D. W. Koopman, *Quantum Electronics, IEEE Journal of*, 1979, **15**, 444-451.
4. W. A. VonDrasek, S. Okajima and J. P. Hessler, *Appl. Opt.*, 1988, **27**, 4057-4061.
5. R. Berman, E. L. Foster and J. M. Ziman, *Proceedings of the Royal Society of London. Series A, Mathematical and Physical Sciences*, 1955, **231**, 130-144.
6. K. A. McCarthy, S. S. Ballard and E. C. Doerner, *Phys. Rev.*, 1952, **88**, 153.
7. G. Herzberg and L. L. Howe, *Can. J. Phys.*, 1959, **37**, 636-659.
8. D. Drouin, A. R. e. Couture, D. Joly, X. Tastet, V. Aimez and R. Gauvin, *SCANNING*, 2007, **29**, 92-101.
9. R. Luna, M. Á. Satorre, M. Domingo, C. Millán and C. Santonja, *Icarus*, 2012, **221**, 186-191.
10. C. J. Bennett, S.-H. Chen, B.-J. Sun, A. H. H. Chang and R. I. Kaiser, *Astrophys. J.*, 2007, **660**, 1588.
11. R. L. Hudson and M. H. Moore, *Icarus*, 2000, **145**, 661-663.
12. S. R. Polo and M. K. Wilson, *J. Chem. Physics*, 1955, **23**, 2376-2377.
13. C. J. Bennett and R. I. Kaiser, *Astrophys. J.*, 2007, **661**, 899-909.
14. R. I. Kaiser, S. Maity and B. M. Jones, *Physical Chemistry Chemical Physics*, 2014,**16**, 3399-3424.
15. E. Herbst and E. F. van Dishoeck, *Annual Review of Astronomy and Astrophysics*, 2009, **47**, 427-480.
16. A. C. A. Boogert, W. A. Schutte, A. G. G. M. Tielens, D. C. B. Whittet, F. P. Helmich, P. Ehrenfreund, P. R. Wesselius, T. de Graauw and T. Prusti, *Astronomy and Astrophysics*, 1996, **315**, L377-L380.
17. E. L. Gibb, D. C. B. Whittet, A. C. A. Boogert and A. G. G. M. Tielens, *The Astrophysical Journal Supplement Series*, 2004, **151**, 35-73.
18. K. I. Öberg, R. T. Garrod, E. F. van Dishoeck and H. Linnartz, *Astronomy and Astrophysics*, 2009, **504**, 891-913.
19. K. I. Oberg, E. F. van Dishoeck and H. Linnartz, 2009.
20. K. I. Öberg, A. C. A. Boogert, K. M. Pontoppidan, B. Saskia van den, E. F. v. Dishoeck, B. Sandrine, A. B. Geoffrey and I. Neal J. Evans, *Astrophys. J.*, 2011, **740**, 109.
21. E. Dartois, W. Schutte, T. R. Geballe, K. Demyk, P. Ehrenfreund and L. D'Hendecourt, *Astronomy and Astrophysics*, 1999, **342**, L32-L35.
22. K. M. Pontoppidan, E. Dartois, E. F. van Dishoeck, W.-F. Thi and L. d'Hendecourt, *Astronomy and Astrophysics*, 2003, **404**, L17-L20.
23. G. A. Blake, E. C. Sutton, C. R. Masson and T. G. Phillips, *Astrophys. J.*, 1987, **315**, 621-645.
24. P. M. Woods, B. Slater, Z. Raza, S. Viti, W. A. Brown and D. J. Burke, *Astrophys. J.*, 2013, **777**, 90.
25. P. M. Woods, G. Kelly, S. Viti, B. Slater, W. A. Brown, F. Puletti, D. J. Burke and Z. Raza, *Astrophys. J.*, 2012, **750**, 19.
26. N. Watanabe and A. Kouchi, *The Astrophysical Journal Letters*, 2002, **571**, L173.

27. N. Watanabe, T. Shiraki and A. Kouchi, *The Astrophysical Journal Letters*, 2003, **588**, L121.
28. A. G. G. M. Tielens and D. C. B. Whittet, eds., *Molecules in Astrophysics: Probes and Processes*, Dordrecht: Kluwer, 1997.
29. S. B. Charnley, A. Tielens and S. D. Rodgers, *The Astrophysical Journal Letters*, 1997, **482**, L203.
30. J. M. Hollis, F. J. Lovas and P. R. Jewell, *The Astrophysical Journal Letters*, 2000, **540**, L107-L110.
31. Y. J. Chen, A. Ciaravella, G. M. M. Caro, C. Cecchi-Pestellini, A. Jimenez-Escobar, K. J. Juang and T. S. Yih, *Astrophys. J.*, 2013, **778**, 162.
32. P. Modica and M. E. Palumbo, *Astronomy and Astrophysics*, 2010, **519**, 22.
33. P. Modica, M. E. Palumbo and G. Strazzulla, *Planetary and Space Science*, 2012, **73**, 425-429.
34. M. T. Beltrán, C. Codella, S. Viti, R. Neri and R. Cesaroni, *The Astrophysical Journal Letters*, 2009, **690**, L93.
35. D. T. Halfen, A. J. Apponi, N. Woolf, R. Polt and L. M. Ziurys, *Astrophys. J.*, 2006, **639**, 237-245.
36. G. W. Fuchs, H. M. Cuppen, S. Ioppolo, C. Romanzin, S. E. Bisschop, S. Andersson, E. F. van Dishoeck and H. Linnartz, *Astronomy and Astrophysics*, 2009, **505**, 629-639.
37. K. Hiraoka, T. Sato, S. Sato, N. Sogoshi, T. Yokoyama, H. Takashima and S. Kitagawa, *Astrophys. J.*, 2002, **577**, 265.
38. N. Watanabe, A. Nagaoka, T. Shiraki and A. Kouchi, *Astrophys. J.*, 2004, **616**, 638.
39. N. Watanabe, A. Nagaoka, H. Hidaka, T. Shiraki, T. Chigai and A. Kouchi, *Planetary and Space Science*, 2006, **54**, 1107-1114.
40. B. M. Jones and R. I. Kaiser, *The Journal of Physical Chemistry Letters*, 2013, **4**, 1965-1971.
41. M. T. Beltrán, R. Cesaroni, R. Neri, C. Codella, R. S. Furuya, L. Testi and L. Olmi, *Astronomy and Astrophysics*, 2005, **435**, 901-925.
42. J. K. Jørgensen, C. Favre, S. E. Bisschop, T. L. Bourke, E. F. van Dishoeck and M. Schmalzl, *The Astrophysical Journal Letters*, 2012, **757**, L4.
43. C. C. Pei, S.-Y. Liu and L. E. Snyder, *Astrophys. J.*, 2000, **530**, 800.
44. S. B. Charnley and S. D. Rodgers, in *IAU Symp. 231*, eds. D. C. Lis, G. A. Blake and E. Herbst, Cambridge: Cambridge Univ. Press, 2005.
45. G. Strazzulla and R. E. Johnson, in *Comets in the Post-Halley Era*, eds. R. L. Newburn, Jr., M. Neugebauer and J. Rahe, Springer Netherlands, 1991, pp. 243-275.
46. M. H. Moore, R. L. Hudson and P. A. Gerakines, *Spectrochimica Acta*, 2001, **57**, 843-858.
47. S. Ptasinska, S. Denifl, P. Scheier and T. D. Mark, *Int. J. Mass Spectrom.*, 2005, **243**, 171-176.
48. F. Turecek and Z. Havlas, *The Journal of Organic Chemistry*, 1986, **51**, 4066-4067.
49. M. E. Jacox and D. E. Milligan, *J. Mol. Spectrosc.*, 1973, **47**, 148-162.
50. E. P. Kalyazin and G. V. Kovalev, *Khim. Vys. Energ.*, 1978, **12**, 371-373.
51. K. Toriyama and M. Iwasaki, *J. Am. Chem. Soc.*, 1979, **101**, 2516-2523.
52. G. A. Baratta, A. C. Castorina, G. Leto, M. E. Palumbo, F. Spinella and G. Strazzulla, *Planetary and Space Science*, 1994, **42**, 759-766.

53. G. Strazzulla, A. C. Castorina and M. E. Palumbo, *Planetary and Space Science*, 1995, **43**, 1247-1251.
54. R. L. Hudson and M. H. Moore, *Radiat. Phys. Chem.*, 1995, **45**, 779-789.
55. P. A. Gerakines, W. A. Schutte and P. Ehrenfreund, *Astronomy and Astrophysics*, 1996, **312**, 289-305.
56. M. H. Moore, R. F. Ferrante and J. A. Nuth Iii, *Planetary and Space Science*, 1996, **44**, 927-935.
57. M. E. Palumbo, A. C. Castorina and G. Strazzulla, *Astronomy and Astrophysics*, 1999, **342**, 551-562.
58. G. A. Baratta, G. Leto and M. E. Palumbo, *Astronomy and Astrophysics*, 2002, **384**, 343-349.
59. R. Brunetto, M. A. Barucci, E. Dotto and G. Strazzulla, *Astrophys. J.*, 2006, **644**, 646-650.
60. A. Ciaravella, G. M. Caro, A. J. Escobar, C. Cecchi-Pestellini, S. Giarrusso, M. Barbera and A. Collura, *The Astrophysical Journal Letters*, 2010, **722**, L45.
61. A. L. F. de Barros, A. Domaracka, D. P. P. Andrade, P. Boduch, H. Rothard and E. F. da Silveira, *Mon. Not. R. Astron. Soc.*, 2011, **418**, 1363-1374.
62. J. E. Bertie and S. L. Zhang, *J. Mol. Struct.*, 1997, **413-414**, 333.